Development of a Fabric-Reinforced Porous Graft for Vascular Tissue Engineering Using Finite Element Methods and Genetic Algorithms

Mark S. Yeoman, B. Daya Reddy, Deon Bezuidenhout, Hellmut C. Bowles, Peter Zilla and Thomas Franz

Abstract Small to medium diameter vascular grafts have met with little success over the past 50 years. Surface thrombogenicity and anastomotic intimal hyperplasia, the main reasons for graft failure, are believed to be governed by a lack of endothelialisation and compliance mismatch between graft and host artery. High-porosity polyurethane grafts allow for cellular ingrowth and vascularization, they however encounter detrimental ballooning and low burst strength. To improve the structural properties, a support is required that will not adversely affect ingrowth permissibility of the graft. In this study, an approach combining finite element methods and genetic algorithms was developed to adopt the concept of arterial mechanics, which are predominantly governed by medial and adventitial layer, to tissue-regenerative vascular grafts. The numerical method was able to identify the mechanical properties of adventitial knit fabrics that optimally complement three different intimal/medial porous polyurethane structures to provide grafts with a

M. S. Yeoman (✉)
Continuum Blue Ltd., Tredomen Innovation and Technology Park, Hengoed, UK
e-mail: mark@continuum-blue.com

B. D. Reddy
Centre for Research in Computational and Applied Mechanics, University of Cape Town, Cape Town, South Africa

D. Bezuidenhout · P. Zilla · T. Franz (✉)
Cardiovascular Research Unit, Chris Barnard Division of Cardiothoracic Surgery, Faculty of Health Sciences, University of Cape Town, Private Bag X3, Observatory, Cape Town 7935, South Africa
e-mail: thomas.franz@uct.ac.za

H. C. Bowles
Finite Element Analysis Services (Pty.) Ltd., Parklands, South Africa

T. Franz
Research Office, University of Cape Town, Cape Town, South Africa

T. Franz
Centre for Research in Computational and Applied Mechanics, University of Cape Town, Cape Town, South Africa

Stud Mechanobiol Tissue Eng Biomater (2014) 15: 29–61
DOI: 10.1007/8415_2013_162

Published Online: 20 June 2013

compliance of 5.3, 5.5 and 6.0 %/100 mmHg. Grafts featuring fabrics manufactured according to the numerically specifications exhibited an in vitro compliance of 2.1 ± 0.8, 3.0 ± 2.4 and 4.0 ± 0.7 %/100 mmHg. Beyond the demonstration of the feasibility of numerical method, it was shown that the graft system of adventitially reinforced polymer with well-defined interconnected porosity can be expected to facilitate the ingrowth and regeneration of vascular tissue for all pore sizes studied.

1 Introduction

Although the mechanisms behind sub-optimal patency and failure of small- to medium-diameter grafts are not fully understood, it is clear that compliance mismatch and the thrombogenetic nature of non-endothelialised surfaces are major contributors [9, 10, 12, 19, 21, 26, 30]. Previous studies have shown that it is a combination of the thrombogenetic nature of the graft material, surface roughness, and the mechanical and hemodynamic properties of the replacement graft in relation to the host artery which add up to the relatively poor performance of prosthetic grafts as compared with vein grafts or arterial grafts [3, 12].

Tissue engineering and regeneration efforts of the past two decades have aimed at the creation of biological interfaces between the blood and the prosthesis. As an alternative to the in vitro endothelialization of conventional vascular prostheses with cultured autologous endothelial cells [6], the concept of transmural endothelialization requires ingrowth-permissive graft structures [11, 12, 15, 30]. Given the defined dimensions of capillaries and arterioles, many of the ill-defined porous structures investigated for this purpose exhibit pore interconnections which are too narrow to allow for complete penetration of the graft wall. Therefore, structures with well-defined interconnected micro-pores and channels have been developed with optimal porosities for both vascular ingrowth and mitigation of inflammation [2]. As much as the biological response patterns seem to require large, open porosity in thin-walled grafts, the resulting structural weakness and the excessive viscoelastic properties may pose a prohibitive obstacle.

Past research has utilized winding methods to reinforce these graft structures [23]. However, these methods cause radial compression, high stress concentrations, excessively reduced compliance and nonlinear effects in the region of the reinforcement. Thus, a better method of reinforcement is required which does not cause localized stress concentrations and hence excessive localized compression of the porous structure while still allowing for tissue regeneration through the support structure.

Fabric or mesh structures may offer advantages in externally reinforcing the porous polymer grafts more uniformly. However, complex mechanics impose a challenge for deriving optimal fabric designs that will, in combination with the porous structures, provide the desired mechanics of the reinforced grafts.

Genetic algorithms (GA) and finite element methods (FEM) have been used to study structural and thermal optimization problems in medicine. Khalil et al. [14] proposed a computational scheme for the elasticity reconstruction of soft tissue.

The scheme comprises finite element (FE) modeling for mechanical analysis with genetic algorithms for parameter estimation, and was successfully applied to the elasticity characterization of atherosclerotic plaques in diseased arteries. A similar approach was followed by Hsu et al. [13] to optimize the design of locking screws used for fracture fixation and bone healing of tibial fractures. The two principal objectives in the design of these orthopedic screws are bending strength and bone holding power. Since these two objectives may conflict with each other, a multi-objective optimization method based on FE modeling and genetic algorithms was used to evaluate and rank various screw designs.

Siauve et al. [20] showed a potential clinical utilization of genetic algorithms coupled with a FE formulation. They developed a treatment tool for local hyperthermia treatment of cancer which optimizes radio-frequency and microwave sources so as to achieve a temperature distribution specific for individual patients. The use of genetic algorithms has also been successfully demonstrated for bio-medical applications. Pandit et al. [18] and Wang et al. [25] utilized GAs for the development of a two-layer three-dimensional constitutive model for porcine coronary arteries. Approximating the arterial wall by an intima-media layer and an adventitial layer, they combined genetic algorithms with experimental testing to determine the material properties of each of the two layers. After testing intact arteries and their corresponding dissected adventitia or intima-media layer, the material properties of the missing layer were computed from the properties of the intact wall and the tested layer.

The aim of this work was to propose the use of an elastic knit fabric structure for the externally, i.e. 'adventitial', reinforcement of a porous polymeric vascular graft [27, 28]. The polymeric structure with well-defined interconnected porosity [1, 2, 5] served as scaffold for tissue integration and regeneration but exhibited low mechanical strength. The adventitial fabric acted as reinforcement for the porous scaffold, providing structural integrity and desired mechanical characteristics of the graft, while permitting cellular activity to take place through its structure. The design of the reinforcing fabric was facilitated with a combination of FE methods and genetic algorithms. The process aimed at the determination of mechanical properties of the fabric structure that, combined with the porous polymeric structure, result in a specific dynamic compliance, nonlinear pressure-diameter response and diastolic diameter of the graft.

2 Development of a Constitutive Model for Warp-Weft Coupled Knitted Fabrics

Knits are fabrics where yarns are inter-looped. Generally, knitted structures are not as stiff as their woven counterparts and are highly porous. Knitted fabrics encompass warp and weft knits. Warp knits, found in many medical implants, are

complex compared to weft knits. Weft knit structures tend to be highly extendible but are structurally unstable, unless interlocking occurs. This interlocking tends to reduce extensibility but does help with elastic recovery. Advantages of knitted fabrics include that being flexible and comfortable in nature, and they tend not to fray or unravel at the edges.

2.1 Formulation of Fabric Constitutive Relationship

Large strain formulations are required when describing coarse knit fabrics under tension. The fabric constitutive model assumed that the material is highly elastic and compressible. Viscoelastic effects were neglected and incompressibility was not enforced. Due to the small thickness compared to the in-plane dimensions of the fabric, plane stress was implemented under consideration of tension and shear deformation. Since the non-linear stress-strain characteristics of fabrics are similar to those of soft tissue, it was proposed to adapt a strain energy function for soft tissue proposed by Chuong et al. [4]:

$$w(E) = \frac{C}{2}\exp\left(a_1 E_{\theta\theta}^2 + a_2 E_{zz}^2 + 2a_4 E_{\theta\theta} E_{zz}\right). \tag{1}$$

By including shear and increasing the number and order of coefficients, the proposed fabric strain energy function in general two-dimensional form was obtained as

$$\begin{aligned} w(E) = \frac{C}{2}\exp\big[&a_1 E_{11}^2 + a_2 E_{22}^2 + a_3\left(E_{12}^2 + E_{21}^2\right) + a_4(E_{11}E_{22}) + a_5 E_{11}^3 \\ &+ a_6 E_{22}^3 + a_7\left(E_{12}^3 + E_{21}^3\right) + a_8\left(E_{11}^3 E_{22}\right) + a_9\left(E_{11}E_{22}^3\right)\big] \end{aligned} \tag{2}$$

where C and a_i ($i = 1$–9) are fabric material coefficients.

An Abaqus® UMAT subroutine was utilized for implementation of the fabric constitutive model. The subroutine provided the material elasticity tensor, stress and solution dependent variable updates at each increment.

The discrete elasticity tensor is defined by

$$K_{ijkl}^{\sigma\varepsilon} = \frac{\partial \sigma_{ij}}{\partial \varepsilon_{kl}}, \tag{3}$$

where σ and ε are the stress and strain, respectively. For large strain computations an appropriate conjugate stress-strain measure is needed. Since the proposed strain energy function is already defined in terms of Green strain E an appropriate conjugate pair is Green strain and the second Piola-Kirchhoff stress S, which are defined as

$$E = \frac{1}{2}\left(\nabla u + (\nabla u)^T + (\nabla u)^T \nabla u\right) \tag{4}$$

and

$$S_{ij} = \frac{\partial w}{\partial E_{ij}}. \tag{5}$$

The stress was explicitly defined as Cauchy 'true' stress using the relationship between Cauchy stress and second Piola-Kirchhoff stress in the form

$$\sigma_{ij} = J^{-1} F_{ik} S_{kl} F_{jl}. \tag{6}$$

Unlike the model by Chuong et al. [4], Eq. (1), incompressibility was not enforced. For the implementation in Abaqus®, the following special conditions were used; *Orientation*: defined the transverse fabric directions to ensure the material properties remained orientated as elements rotated and deformed; *Membrane element thickness*: A thickness of 100 μm was assigned to the membrane elements that were used to model the fabric; *Poisson's ratios* υ_{13} *and* υ_{31}: The use of membrane elements ensured a state of plane stress, thus the thickness was assumed to be constant.

2.2 Assessment of Model Parameters and Verification of Constitutive Relationship

Single and multiple element patch tests were utilized to assess the influence of the material coefficients (C, a_1, a_2, a_3, a_4, a_5, a_6, a_7, a_8 and a_9) and the effects of element orientation and type under uniaxial tensile and simple shear deformation. The single element models used a four-noded bilinear membrane element with boundary and load conditions describing the two modes of deformation, as illustrated in Fig. 1a, b. Arbitrary fabric coefficients were employed and varied slightly to observe their influence on stress and strain behaviour. The effect of element type and orientation was assessed, in tension and shear, with a uniform mesh with consistently ordered four-noded membrane elements and a non-uniform mesh with three and four-noded membrane elements, Fig. 1c, d.

Figure 2 displays the stress-strain curves and the normalized stress, obtained from dividing the stress values obtained at 20 % tensile strain and 10 % shear strain by the stress values achieved with that of the model with $C = 10000$ and $a_i = 10$. The numerically predicted stress-strain curves (Fig. 2a) exhibit a nonlinear stiffening effect characteristic for fabrics. Defining the subscripts i and j to denote the direction of uniaxial tension and the transverse direction, respectively, the following was observed (Note: The results in Fig. 2 are for $i = 2$ being the direction of uniaxial tension). As expected, the magnitude of stress increased proportionately with C. The *nonlinear stiffening effect*: greatly increased with increasing coefficients that affect terms containing E_{ii}^2, i.e. a_1 and a_2; moderately increased with increasing coefficients that affect terms E_{ii}^3, i.e. a_6; slightly increased with

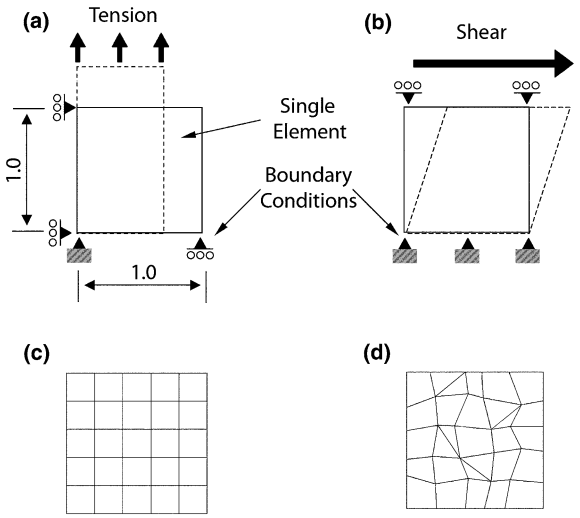

Fig. 1 Patch test models: Single element models for **a** uniaxial tension and **b** simple shear; Multi element models with **c** uniform and **d** non-uniform mesh

increasing coefficients that affect $E_{jj}^3 E_{ii}$, i.e. a_8; greatly decreased with increasing coefficients affecting $E_{ii}E_{jj}$, i.e. a_4; slightly decreased with increasing coefficients that affect E_{jj}^3 and $E_{jj}E_{ii}^3$, i.e. a_5 and a_9; and was not affected by changing coefficients that affect E_{ij}, i.e. a_3 and a_7. The effect of changing a_1 through a_9 depended on the power of the strain terms to which they contribute. Those that affect lower order terms had a larger influence, as expected.

Further information was gained from the normalized stress and the associated transverse strain (Fig. 2b). The magnitude of axial and transverse stress was proportional to C; however, transverse strain was not affected by C. The *transverse strain, or Poisson's effect*: increased with increasing coefficients that affect product terms $E_{jj}E_{ii}$ and $E_{jj}E_{ii}^3$, i.e. a_4 and a_9; decreased with increasing coefficients that affect E_{jj}^2, E_{jj}^3 and $E_{jj}^3 E_{ii}$, i.e. a_1, a_5 and a_8; and was not affected by a_2, a_3, a_6 and a_7. The *axial and transverse stress*: both increased with increasing coefficients that a_2 and a_6 that affect terms E_{ii}^2 and E_{ii}^3, with axial stress being dominant; both decreased with increasing a_4, a_5, a_8 and a_9, with a predominant change in transverse stress for the latter two; and increased and decreased, respectively, with increasing coefficients that affect E_{jj}^2, i.e. a_1. Negative coefficients a_i typically reduced transverse strain. A negative a_4 produced a negative normalized transverse strain, indicating positive strains in this direction. Negative a_2 and a_6 reduced the stress values but did not affect the transverse strain. Negative a_4 and a_9 increased the axial stress while reducing the transverse stress. Negative a_5 did not change the axial stress but reduced the transverse stress. Negative a_2 and a_6 caused compressive axial stress whilst in tension, which is unrealistic. Negative a_8 reduced both the axial and transverse stress values considerably. Negative a_7 did not affect the stress and transverse strain.

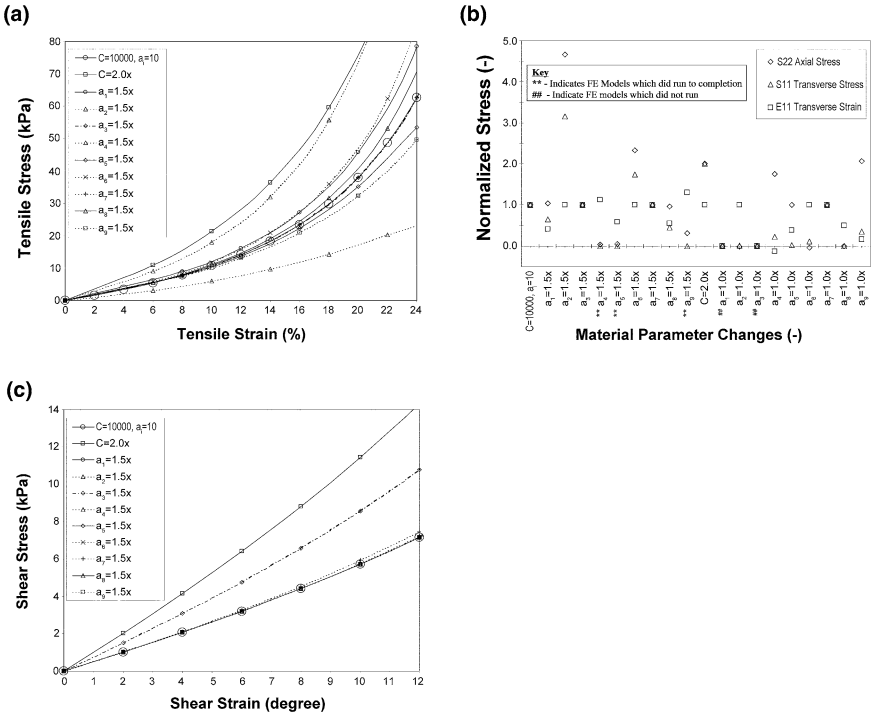

Fig. 2 Effects of fabric material coefficients C and a_i: **a** Stress-strain curves and **b** normalized stress and transverse strain for uniaxial tension; **c** Shear stress–shear angle curves

Figure 2c shows typical curves of shear stress versus shear angle obtained from the simple shear model. Although not clearly observed, the shear stress-strain relation became slightly curved by increasing coefficients a_3 and a_7. Table 1 summarizes the results of the comparative tests with the uniform and non-uniform multi-element models and the single element model for uniaxial tensile and simple shear.

2.3 Implementation and Validation of Fabric Constitutive Model

To assess the ability of the constitutive model to simulate the physical fabric mechanics, four distinctly different fabrics were obtained (Finitex (Pvt.) Ltd., Cape Town, South Africa): (1) basic warp knit, (2) warp knit with Lycra® support, (3) coarse warp knit and (4) monofilament warp knit. The selected fabrics were part of standard production lots that underwent routine quality assessment with regard to consistency. Figure 3 provides scanning electron micrographs of the fabrics.

Table 1 Patch test results for uniform and non-uniform multi-element model and single element model for uniaxial tension and simple shear

	Multi element uniform	Multi element non-uniform	Single element
Tensile			
$S11$ (Pa)	6.776	6.776	6.776
$S22$ (Pa)	0.168×10^7	0.168×10^7	0.168×10^7
$S12$ (Pa)	0	0	0
$U1$ (mm)	−0.581	−0.581	−0.581
Shear			
$S11$ (Pa)	$-0.24 \times 10^5 \rightarrow 1.75 \times 10^5$	$-0.23 \times 10^5 \rightarrow 1.73 \times 10^5$	0.41×10^5
$S22$ (Pa)	$-0.188 \times 10^5 \rightarrow 4.92 \times 10^5$	$-0.193 \times 10^5 \rightarrow 4.82 \times 10^5$	0.59×10^5
$S12$ (Pa)	$0.072 \times 10^5 \rightarrow 2.86 \times 10^5$	$0.097 \times 10^5 \rightarrow 2.81 \times 10^5$	0.86×10^5

Ranges are given for the simple shear test. Notations: $S11$, $S22$ Normal stress in 1 and 2 directions; $S12$ Shear stress; $U1$ Displacement in 1 direction

Uniaxial tensile tests were performed on samples with dimensions 60 × 20 mm at 37 °C (Instron® 5544, Instron Corp., Norwood, MA), see Fig. 4a. The loading protocol comprised: (1) Pre-load to 1 % nominal strain at a strain rate of 50 mm/min to reduce material inconsistencies, and (2) Extension to 50 % nominal strain at a strain rate of 200 mm/min, the strain rate stipulated by medical implant standards [16, 17]. Due to difficulties in monitoring lateral strain effects during the Instron® tests, caused by curling effects at the sample edges, fabric samples were strained on a flat bed at 37 °C in steps of 10, 20 and 30 %. For both the Instron® and the flat bed tests, a 5 × 5 mm grid was marked on each sample to visualize localized strain effects. Strengthening stitches were sewn at both ends of the samples to minimize localized stress concentrations. Using digital images recorded during the tests, the longitudinal and transverse strain was determined from a single grid cell located in the center of the sample.

A quarter-symmetric FE model was used to simulate the physical uniaxial tensile tests. The model, see Fig. 4b, utilized a mesh of four-noded membrane elements. The boundary conditions were selected such that edge AB was free to move horizontally but constrained vertically, while edges AD and DC were free to move vertically but constrained horizontally. A quasi-static displacement at 200 mm/min [16, 17] was applied to edge DC. The loaded boundary DC and the edge BC were expected to have a greater variation in stress and deformation. Hence the element mesh was refined toward these edges. The mesh sensitivity was assessed by increasing and biasing the element density toward edges BC and DC and center point A until the stress, strain and displacement fields became consistent.

2.3.1 Optimisation of Fabric-Specific Constitutive Coefficients

A genetic algorithm GA1, programmed using Perl®, was utilized to iteratively optimize the fabric model coefficients to represent the physically tested fabrics. Using a single set of fabric coefficients, GA1 ran mutually orthogonal uniaxial

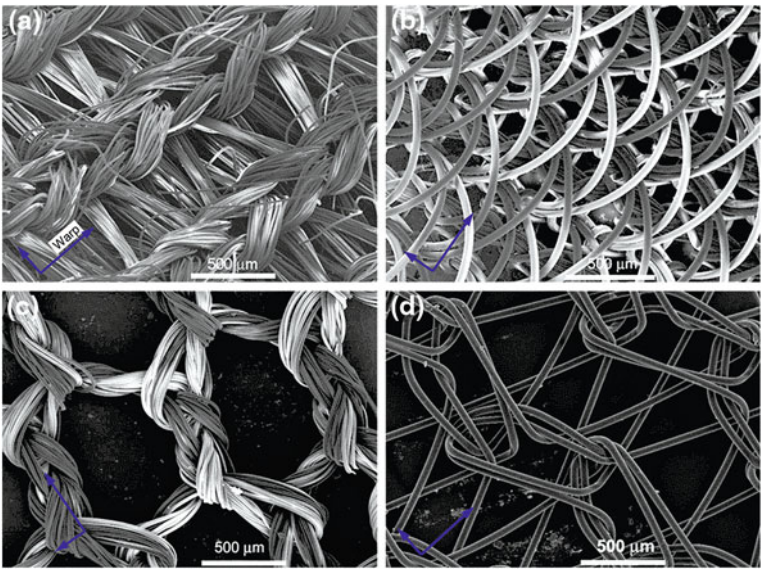

Fig. 3 Scanning electron micrographs (50x) of fabrics tested with arrows indicating warp and weft directions. **a** Basic warp knit (sample 1), **b** Warp knit with Lycra® support (sample 2), **c** Coarse warp knit (sample 3) and **d** Monofilament warp knit (sample 4)

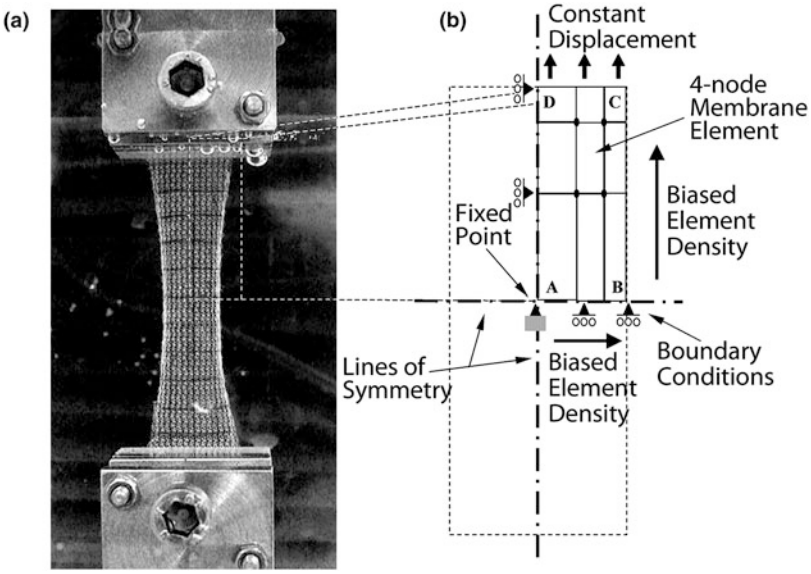

Fig. 4 **a** Photograph of fabric sample and customized clamps during uniaxial tensile test and **b** Schematic of FE model for uniaxial tensile test utilizing symmetry

tensile FE models in order to predict stress-strain curves for the warp and weft directions. Subsequently, GA1 analyzed the predicted results with respect to the fit with physical test data utilizing objective, penalty and fitness functions. This process was repeated until a desired fitness value $f(C, a_i)$ was achieved or when 50 generations were reached.

Dynamic Range and Resolution of the Search Space

The search space of GA1 was dynamically confined and refined over the generations. An initial large range with low resolution allows GA1 to maximize its initial search over a wide search space. With increasing generations, the range of the search space was reduced and the resolution was increased, in order to constrain GA1 for the refinement of the acceptable solutions obtained. Using initial values of $C = 10000$ and $a_i = 10$ (i = 1–9), the initial search ranges, $\{R\}$, of $0 < C \leq 20000$ and $0 < a_i \leq 20$ (i = 1–9) were biased 3:2 between the first and second ranked solutions of the previous generation. In addition, the search space range was reduced linearly by 2.5 % over each generation. An explicit constraint for the search space range of C ensured that its value remained positive over the generations, $C|C > 0$, to prevent unrealistic compressive or zero stress solutions under tensile strain of the fabric.

The resolution of the search space was increased after each generation. A binary number of m bit was used to encode each scaled coefficient into the chromosome. With the initial value of $m = 5$, the resolution of the search space, $\{R\}/2^m$, was $20/2^5 = 0.625$ for a_i and $20000/2^5 = 625$ for C. The bit size was increased by 1 every 10th generation, reaching $m = 10$ at the 50th generation. Consequently, the range $\{R\}$ was reduced by 50 %, the final resolution was $10/2^{10} = 9.7656 \times 10^{-3}$ for a_i and $10000/2^{10} = 9.7656$ for C. Figure 5 illustrates the reduction of the range and increase of the resolution of a two-dimensional parameter search space.

Objective, Penalty and Fitness Functions

The same set of fabric material model coefficients were utilized in two FE models that describe uniaxial tension in the warp and weft direction, respectively. This was implemented in the FE model by swapping the material model coefficients a_1 with a_2, a_5 with a_6, and a_8 with a_9. For the warp and weft directions, the numerical results for axial stress ($\sigma_{A,i}^{Model}$), localized axial strain ($\varepsilon_{A,i}^{Model}$), and localized transverse strain ($\varepsilon_{T,i}^{Model}$) were compared with the equivalent physical data of axial stress ($\sigma_{A,i}^{Data}$), localized axial strain ($\varepsilon_{A,i}^{Data}$) and localized transverse strain ($\varepsilon_{T,i}^{Data}$) at pre-defined axial strains of 10, 20 and 30 %.

Partial Objective and Penalty Functions

The partial objective functions were calculated from the normalized differences between the model and physical data. The partial objective functions for stress were

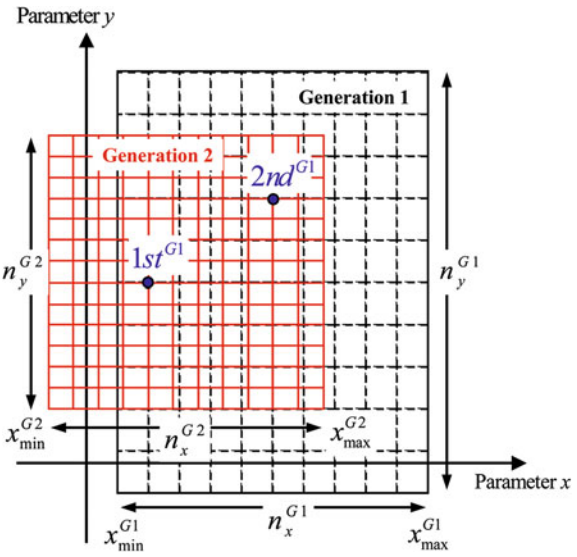

Fig. 5 Schematic illustrating the reduction of a two-dimensional parameter search space from $(x_{\max}^{G1} - x_{\min}^{G1})$ to $(x_{\max}^{G2} - x_{\min}^{G2})$, biased 3:2 between the first and second ranked solutions of generation 1 ($1st^{G1}$, $2nd^{G1}$) and the resolution of the search increased from n_x^{G1} to n_x^{G2} for parameter x and n_y^{G1} to n_y^{G2} for parameter y

$$\phi^{\sigma_A^n} = \frac{\sum_{i=10\,\%,10\,\%}^{30\,\%} w_{\sigma_{A,i}}^n \left[1 - \left\{\left|\triangle\sigma_{A,i}^n\right|\left(\frac{1}{m_{\sigma_{A,i}}^n - 1}\right)\right\}\right]}{\sum_{i=10\,\%,10\,\%}^{30\,\%} w_{\sigma_{A,i}}^n}, \tag{7}$$

with

$$\triangle\sigma_{A,i}^n = \frac{\sigma_{A,i}^{Model,n} - \sigma_{A,i}^{Data,n}}{\sigma_{A,i}^{Data,n}}, \tag{8}$$

and

$$m_{\sigma_{A,i}}^n = \left\{ \begin{array}{ll} 1 + \left|\frac{\sigma_{A,i}^{\max,n} - \sigma_{A,i}^{Data,n}}{\sigma_{A,i}^{Data,n}}\right| & \text{for } \sigma_{A,i}^{Model,n} > \sigma_{A,i}^{Data,n} \\ 1 + \left|\frac{\sigma_{A,i}^{\min,n} - \sigma_{A,i}^{Data,n}}{\sigma_{A,i}^{Data,n}}\right| & \text{for } \sigma_{A,i}^{Model,n} \leq \sigma_{A,i}^{Data,n} \end{array} \right\}. \tag{9}$$

where n is the direction of the uniaxial tensile test (warp or weft), i the pre-defined axial strains of 10, 20 and 30 %, $w_{\sigma_{A,10\,\%}}^n = 6$, $w_{\sigma_{A,20\,\%}}^n = 4$ and $w_{\sigma_{A,30\,\%}}^n = 1$ are the weightings for the pre-defined axial strain field values.

Similarly, the partial objective functions for localized axial strains were

$$\phi^{\varepsilon_A^n} = \frac{\sum_{i=10\,\%,10\,\%}^{30\,\%} w_{\varepsilon_{A,i}}^n \left[1 - \left\{\left|\triangle\varepsilon_{A,i}^n\right|\left(\frac{1}{m_{\varepsilon_{A,i}}^n - 1}\right)\right\}\right]}{\sum_{i=10\,\%,10\,\%}^{30\,\%} w_{\varepsilon_{A,i}}^n} \tag{10}$$

where

$$\triangle\varepsilon_{A,i}^{n} = \frac{\varepsilon_{A,i}^{Model,n} - \varepsilon_{A,i}^{Data,n}}{\varepsilon_{A,i}^{Data,n}}, \tag{11}$$

$$m_{\varepsilon_{A,i}}^{n} = \left\{ \begin{array}{ll} 1 + \left| \frac{\varepsilon_{A,i}^{\max,n} - \varepsilon_{A,i}^{Data,n}}{\varepsilon_{A,i}^{Data,n}} \right| & \text{for } \varepsilon_{A,i}^{Model,n} > \varepsilon_{A,i}^{Data,n} \\ 1 + \left| \frac{\varepsilon_{A,i}^{\min n} - \varepsilon_{A,i}^{Data,n}}{\varepsilon_{A,i}^{Data,n}} \right| & \text{for } \varepsilon_{A,i}^{Model,n} \leq \varepsilon_{A,i}^{Data,n} \end{array} \right\}. \tag{12}$$

The partial objective functions for local transverse strains were

$$\phi^{\varepsilon_T^n} = \frac{\sum_{i=10\,\%,10\,\%}^{30\,\%} w_{\varepsilon_{T,i}}^{n} \left[1 - \left\{ \left| \triangle\varepsilon_{T,i}^{n} \right| \left(\frac{1}{m_{\varepsilon_{T,i}}^{n} - 1} \right) \right\} \right]}{\sum_{i=10\,\%,10\,\%}^{30\,\%} w_{\varepsilon_{T,i}}^{n}}, \tag{13}$$

where

$$\triangle\varepsilon_{T,i}^{n} = \frac{\varepsilon_{T,i}^{Model,n} - \varepsilon_{T,i}^{Data,n}}{\varepsilon_{T,i}^{Data,n}}, \tag{14}$$

$$m_{\varepsilon_{T,i}}^{n} = \left\{ \begin{array}{ll} 1 + \left| \frac{\varepsilon_{T,i}^{\max,n} - \varepsilon_{T,i}^{Data,n}}{\varepsilon_{T,i}^{Data,n}} \right| & \text{for } \varepsilon_{T,i}^{Model,n} > \varepsilon_{T,i}^{Data,n} \\ 1 + \left| \frac{\varepsilon_{T,i}^{\min,n} - \varepsilon_{T,i}^{Data,n}}{\varepsilon_{T,i}^{Data,n}} \right| & \text{for } \varepsilon_{T,i}^{Model,n} \leq \varepsilon_{T,i}^{Data,n} \end{array} \right\}. \tag{15}$$

The differences $\triangle\sigma_{A,i}^{n}$, $\triangle\varepsilon_{A,i}^{n}$ and $\triangle\varepsilon_{T,i}^{n}$ were normalized and weighted to ensure that those solutions which model the test results accurately at lower strains were retained for further generations. The partial objective values tended to unity as model stresses, localized axial and transverse strains tended toward physical data. Similarly, parameters $m_{\sigma_{Ai}}^{n}$, $m_{\varepsilon_{Ai}}^{n}$ and $m_{\varepsilon_{Ti}}^{n}$ were multiples used to bias future generations from a certain side and partially penalize their respective partial objective functions.

The partial penalties and weightings for GA1 were as follows:

$$\text{if } \left\{ \sigma_{A,i}^{n} | \sigma_{A,i} \leq \sigma_{A,i}^{\min,n} \text{ and } \sigma_{A,i} \geq \sigma_{A,i}^{\max,n} \right\} \text{ then } \phi^{\sigma_A^n} \text{ negatively weighted;} \tag{16}$$

$$\text{if } \left\{ \varepsilon_{A,i}^{n} | \varepsilon_{A,i}^{n} \leq \varepsilon_{A,i}^{\min,n} \text{ and } \varepsilon_{A,i}^{n} \geq \varepsilon_{A,i}^{\max,n} \right\} \text{ then } \phi^{\varepsilon_A^n} \text{ negatively weighted;} \tag{17}$$

$$\text{if } \left\{ \varepsilon_{T,i}^{n} | \varepsilon_{T,i}^{n} \leq \varepsilon_{T,i}^{\min,n} \text{ and } \varepsilon_{T,i}^{n} \geq \varepsilon_{T,i}^{\max,n} \right\} \text{ then } \phi^{\varepsilon_T^n} \text{ negatively weighted;} \tag{18}$$

$$w_{x,10\,\%}^{n} > w_{x,20\,\%}^{n} > w_{x,30\,\%}^{n}. \tag{19}$$

In Eq. (19), x represents either axial stress σ_A, localized axial strain ε_A, or localized transverse strain ε_T. This ensured that numerical models which did not run to completion were weighted accordingly. Tests that failed to reach 10 % axial strain were given a lower ranking to those which reached an axial strain of 20 %, similarly for 20 and 30 %, thus favoring those models which ran to completion.

Global Objective, Penalty and Fitness Function

The objective function was represented in terms of the partial objective functions by

$$\phi = \frac{w_{obj}^{\sigma_A^{Warp}} \phi^{\sigma_A^{Warp}} + w_{obj}^{\sigma_A^{Weft}} \phi^{\sigma_A^{Weft}} + w_{obj}^{\varepsilon_A^{Warp}} \phi^{\varepsilon_A^{Warp}} + w_{obj}^{\varepsilon_A^{Weft}} \phi^{\varepsilon_A^{Weft}} + w_{obj}^{\varepsilon_T^{Warp}} \phi^{\varepsilon_T^{Warp}} + w_{obj}^{\varepsilon_T^{Weft}} \phi^{\varepsilon_T^{Weft}}}{w_{obj}^{\sigma_A^{Warp}} + w_{obj}^{\sigma_A^{Weft}} + w_{obj}^{\varepsilon_A^{Warp}} + w_{obj}^{\varepsilon_A^{Weft}} + w_{obj}^{\varepsilon_T^{Warp}} + w_{obj}^{\varepsilon_T^{Weft}}}, \tag{20}$$

where w_{obj}^{i} are pre-defined weightings and i represents the partial objective function to which the weightings apply. These weightings were used to bias the objective value to either the warp or weft direction, to stresses, to localized axial and or transverse strains. From Eq. (20), ϕ tends to unity as $\phi^{\sigma_A^{Warp}}$, $\phi^{\sigma_A^{Weft}}$, $\phi^{\varepsilon_A^{Warp}}$, $\phi^{\varepsilon_A^{Weft}}$, $\phi^{\varepsilon_T^{Warp}}$ and $\phi^{\varepsilon_T^{Weft}}$ tend to unity. The pre-defined values of the weightings are $w_{obj}^{\sigma_A^{Warp}} = w_{obj}^{\sigma_A^{Weft}} = 200$, $w_{obj}^{\varepsilon_A^{Warp}} = w_{obj}^{\varepsilon_A^{Weft}} = 10$ and $w_{obj}^{\varepsilon_T^{Warp}} = w_{obj}^{\varepsilon_T^{Weft}} = 100$.

The global penalty functions, p, were defined as

$$\text{if } \sigma_{A,10\,\%}^{n} \leq 0 \text{ then } p = -\infty \text{ else } p = 1, \tag{21}$$

$$\text{if } \sigma_{T,10\,\%}^{n} \leq 0 \text{ then } p = -\infty \text{ else } p = 1, \tag{22}$$

$$\text{if } \varepsilon_{T,10\,\%}^{n} \geq 0 \text{ then } p = -\infty \text{ else } p = 1, \tag{23}$$

and ensure that the models run and the results obtained are reasonable and acceptable.

The fitness function, f, for the comparison of model solutions and physical data for warp and weft uniaxial tension was:

$$f = p \times \phi. \tag{24}$$

2.3.2 Optimised Model Solutions

For the four fabric samples, convergence of GA1 on a set of single solutions was found after 47, 42, 39 and 45 generations, respectively. Table 1 provides the model coefficients and the fitness, objective and partial objective values obtained from GA1 for each fabric. The fitness values coincided with the objective values, all of which closely approached unity. The average partial objective values obtained for

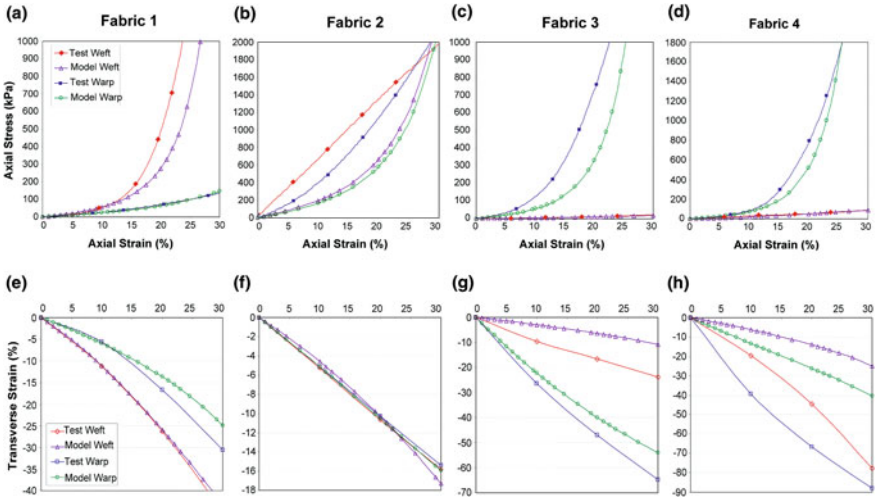

Fig. 6 Nominal stress and engineering strain data of physical tensile tests and model predictions for the warp and weft direction of fabrics 1 to 4: **a–d** Uniaxial tensile stress versus axial strain, **e–h** Transverse strain versus axial strain

fabrics 1 to 4 were 0.99976 ± 0.00020, 0.99971 ± 0.00021, 0.99973 ± 0.00026 and 0.99968 ± 0.00027, respectively.

Figure 6 compares model predictions, obtained using the coefficients identified with GA1, see Table 2, for the axial nominal stress versus axial engineering strain (Fig. 6a–d) and transverse engineering strain versus axial engineering strain (Fig. 6e–h) with data obtained from physical tests. For experimental axial stress and axial strain, fabric samples 1, 3 and 4 exhibited a high degree of anisotropy and nonlinear stress-strain relationships in both the warp and weft directions, see Fig. 6 a, c, d. For these three fabrics, the model solutions fit very well to test data in either warp direction (fabric 1) or weft direction (fabrics 3 and 4), while a reasonable fit between model and test data was obtained in the respective transverse direction. For fabric 2, the physical test data indicated a nearly linear stress-strain relationship in the weft direction and a lower degree of anisotropy (Fig. 6b). Considerable deviation was observed between the model and physical data for this fabric. For transverse strain versus axial strain, fabric 1 exhibited a difference between model and test data of $<1.2\,\%$ in weft direction and $<20\,\%$ in warp direction (Fig. 6e). Close correlation between model and test was obtained for fabric 2 (Fig. 6f), with differences of <1 and $1.5\,\%$ in the warp and weft direction, respectively. However, the solution for fabric 2 was largely linear, while fabric 1 showed an increase in Poisson's effect with an increase in axial strain. Large differences were observed for fabric 3 (Fig. 6g) and fabric 4 (Fig. 6h), except for the weft direction for fabric 3 with a small difference between model and test data of $<2\,\%$ in transverse strain.

Table 2 Model coefficients for fabric samples and associated values for the partial objective functions, objective function and fitness function obtained with the genetic algorithm and the number of generations required to obtain the presented solution

Fabric sample	1	2	3	4
Constitutive coefficients				
C	26444.0	9766.2	12401.0	10299.0
a_1	9.6714	12.77	38.689	81.086
a_2	15.815	15.414	5.2838	35.152
a_3	86.94	12.895	25.122	39.747
a_4	15.742	12.322	19.878	84.289
a_5	−3.8816	2.3294	−9.9038	−22.657
a_6	21.377	−5.3519	0.92224	20.526
a_7	−39.528	−13.246	28.778	43.484
a_8	−5.0215	5.1202	10.485	94.932
a_9	8.5257	−1.9179	12.086	124.26
Fitness value $f(C, a_i)$	0.99985	0.99962	0.99968	0.99970
Objective value $\phi(C, a_i)$	0.99985	0.99962	0.99968	0.99970
Partial objective values				
$\phi^{\sigma_A^{warp}}$	0.99980	0.99957	0.99998	0.99998
$\phi^{\sigma_A^{weft}}$	0.99993	0.99938	0.99947	0.99974
$\phi^{\varepsilon_A^{warp}}$	0.99972	0.99981	0.99989	0.99987
$\phi^{\varepsilon_A^{weft}}$	0.99938	0.99967	0.99991	0.99980
$\phi^{\varepsilon_T^{warp}}$	0.99991	0.99987	0.99935	0.99934
$\phi^{\varepsilon_T^{weft}}$	0.99981	0.99993	0.99979	0.99935
Generation	47	42	39	45

3 Constitutive Modelling of Porous Polymeric Scaffolds

The porous scaffolds featuring well-defined, interconnected pores, see Fig. 7, were manufactured using a biostable ether-free aliphatic segmented polyurethane (PUR) [24] and extractable highly regular spherical porogen (gelatin micro-spheres, Thies Technologies, St. Louis, MO, USA) of three different nominal size ranges of 90–106, 106–125, and 125–150 µm. On average, the pores created in the polyurethane structure were 1.21 ± 0.07 times the diameter of the porogen from which they were formed, while the interconnecting windows were 0.52 ± 0.04 times the diameter [1].

A hyperfoam strain energy function ψ [22] was used to describe the porous polymer:

$$\psi\left(\bar{\lambda}_1, \bar{\lambda}_2, \bar{\lambda}_3\right) = \sum_{i=1}^{N} \frac{2\mu_i}{\alpha_i^2}\left[\left(\bar{\lambda}_1^{\alpha_i} + \bar{\lambda}_2^{\alpha_i} + \bar{\lambda}_3^{\alpha_i} - 3\right) + 3\left(J^{-\frac{1}{3}\alpha_i} - 1\right) + \frac{1}{\beta_i}\left(J^{-\alpha_i\beta_i} - 1\right)\right]. \tag{25}$$

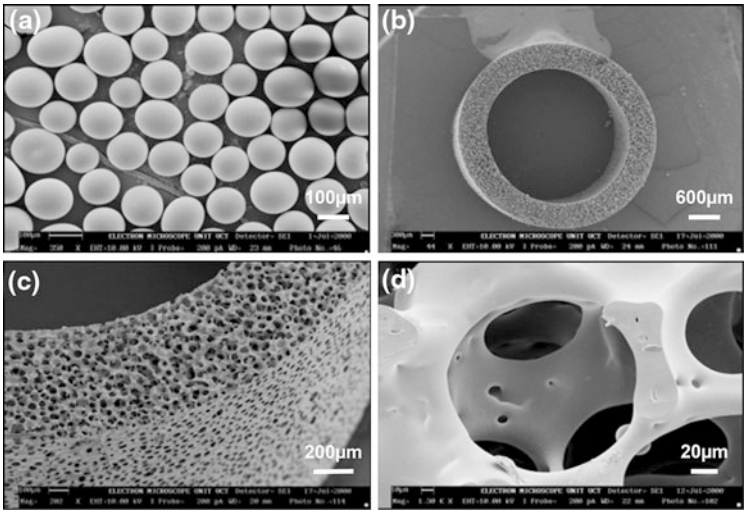

Fig. 7 SEM images of **a** porogens gelatin microspheres, **b** porous graft cross-section, **c** porous graft wall and **d** porous structure [29]

Here $\lambda_k (k = 1, 2, 3)$ are the principal stretches, J is the Jacobian of the deformation gradient and represents the ratio of current to initial volume change, $\overline{\lambda}_i = J^{1/3}\lambda_i$ are deviatoric stretches, and α_i, β_i, and μ_i are material constants.

The material model was validated through experimental tensile, compressive and shear tests. The tests were performed under physiological conditions on unit disk samples of the porous PUR of the various porogen size groups. The experimental and numerical data agreed well for tensile strain below 55 % and compressive strain below 30 %. Since the porous structures experience a maximum tensile strain of about 30 % under physiological conditions, these limits were not deemed problematic.

4 Development and Optimisation of Reinforced Graft System

4.1 Finite Element Models and Optimisation Algorithm

4.1.1 Graft FE Model

The graft model was used to find the static and dynamic compliance values and pressure-diameter curves for different adventitial reinforcing fabric material model coefficients C and $a_i (i = 1, \ldots, 9)$, Eq. (3), with a particular porous graft. Figure 8 illustrates the element, boundary and load conditions used for the graft model. The model simulates the behaviour of the porous graft structure reinforced externally

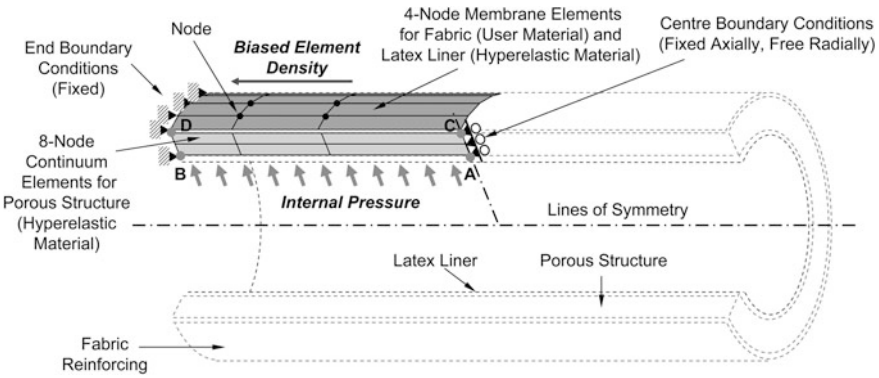

Fig. 8 Graft FE model

with the fabric reinforcing. Due to the symmetry of the problem, only one half of the longitudinal section of the graft and a quarter of the graft in the circumferential direction was modelled.

Eight-node continuum elements without twist were used to model the porous polymer structure, while four-node linear membrane elements without twist were used for the fabric reinforcing. Two load cases were utilized to simulate static and dynamic compliance loads. In both cases, a pre-defined longitudinal (axial) strain of 10 % was initially applied before an internal pressure was applied on the inner surface of the porous structure. For the static load case the internal pressure applied to the inner graft surface was linearly ramped from 0 to 300 mmHg (39996 Pa) over 30 s. This mimicked the physical static compliance test carried out on a graft. For the dynamic load case, the internal pressure on the graft lumen wall was linearly ramped from 0 to 100 mmHg (13332 Pa) over a period of 4 s, after which a pulsatile pressure wave, described by a seven-term Fourier series

$$\begin{aligned} \alpha &= A_o + \sum_{1}^{6} (B_n \sin n\varpi(t - t_o)) \quad \text{for } t \geq t_o, \\ \alpha &= A_o \quad \text{for } t < t_o, \end{aligned} \tag{26}$$

was applied to mimic the pressure pulse applied in physical studies. Here ϖ is the frequency ($\varpi = 15.14$ rad/s and period $T = 0.83$ s), t_o the time at which cyclic load starts ($t_o = 0$), A_o the initial amplitude ($A_o = 13332$ Pa), and B_n are the Fourier constants ($B_1 = 2418.5$, $B_2 = 691.0$, $B_3 = 230.33$, $B_4 = 115.17$, $B_5 = B_6 = 114.7$).

Symmetric boundary conditions were applied to the graft model, with the end nodes fully fixed, and the central nodes fixed in the axial direction, allowing no angular twist, while being free to move radially. The graft element mesh was refined longitudinally towards the fixed end, but remained uniform in the radial and circumferential directions. The level of mesh refinement was verified through mesh sensitivity studies ensuring acceptable numerical accuracy.

4.1.2 Fabric FE Models

The circumferential and longitudinal tensile models were used to provide mutually orthogonal stress-strain curves of the optimized fabric reinforcing solution obtained from the graft model and the genetic algorithm. The stress-strain curves obtained from the circumferential and longitudinal models were then used to produce reinforcing fabrics for the physical studies. The FE model corresponding to experimental circumferential tensile test performed on fabrics at 37 °C is illustrated in Fig. 9a. Due to the geometry of the problem and loading conditions, a 1/8 symmetric model was analysed. Two steps were used in the circumferential tensile model: an initial contact step, which established contact between the analytically rigid pin and the fabric, and a second step which displaced the top pin at a rate of 200 mm/min [16, 17], until 50 % circumferential strain was obtained. A 'soft' contact model was used which takes the form of an exponential function for the pressure-clearance relation. This allowed for the gradual transfer of load from the pin to fabric. The pin was assumed to be smooth and frictionless. The orientations of the optimized material properties obtained from the graft model solutions were mapped onto the membrane elements, ensuring that the fabric principal directions were in-plane with the membrane surface. Longitudinal fabric sample lengths of 48.0 mm were clamped flat at the ends and subjected to uniaxial tension. Figure 9b shows the full and quarter symmetric FE model used to obtain curves of force per unit length vs. displacement curves for the fabric reinforcing in the longitudinal direction. The longitudinal tensile model used a single step, which displaced the end of the fabric tube at a strain rate of 200 mm/min [16, 17] to 100 % axial strain.

A mesh refinement study was performed for each FE model. Critical nodes were monitored and mesh density was increased until the stress, strain and displacements observed became stable and consistent, thus reducing the error in model solutions.

4.1.3 Genetic Algorithm for Graft Optimization Procedure

A genetic algorithm GA2 was used to optimize the fabric model coefficients $C, a_i (i = 1, \ldots, 9)$ in Eq. (3) to obtain a dynamic compliance C_d of 6 %/100 mmHg, a diastolic diameter d_{dia} of 4.0 mm, and to display non-linear stiffening from a dynamic graft FE model. The FE analysis was executed with a particular fabric model with penalty and fitness functions of GA2. The process was repeated until a desired result was obtained or a pre-defined number of generations were reached. A number of 'good' solutions were then kept over the generations, and were then utilized in the tensile test models to obtain a range of circumferential and longitudinal stress-strain curves for possible physical solutions for the fabric reinforcing.

As for GA1, the search space of GA2 was dynamically adjusted over the generations; an initial range was set for each coefficient and thereafter the range was biased 3:2 between the first and second ranked solutions for the generation. The range of the search space was also reduced linearly, confining and refining the

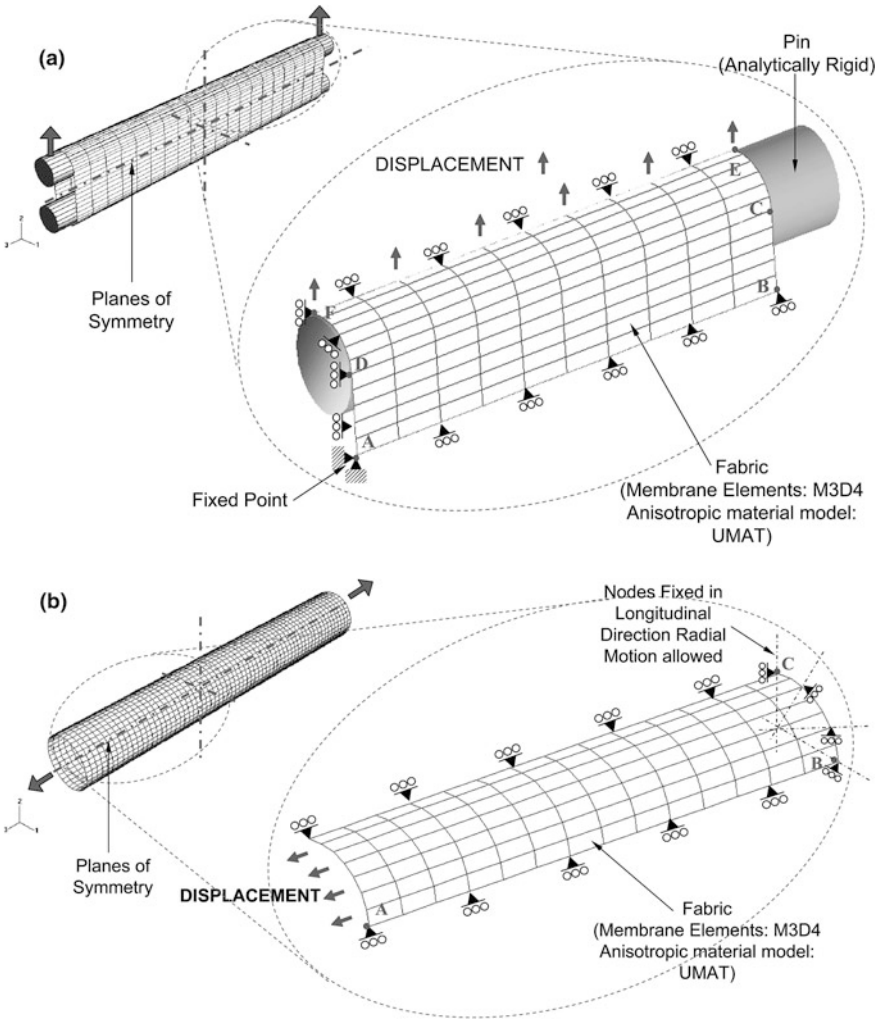

Fig. 9 Quarter-symmetric FE mesh for circumferential (**a**) and longitudinal (**b**) tensile test simulation

search area after each generation. The initial search space coefficient ranges were $0 < C \leq 20000$ and $0 < a_i \leq 20$, with the initial values $C = 10000$ and $a_i = 10$.

The compliance C_d and non-linear stiffening characteristic J were calculated according to

$$C_d = \frac{d_{sys} - d_{dia}}{d_{dia}} \times \frac{100}{P_{sys} - P_{dia}} \times 100, \tag{27}$$

$$J = \frac{(d_{dia} - d_{init})(P_{sys} - P_{dia}) - P_{dia}(d_{sys} - d_{dia})}{P_{dia}}. \tag{28}$$

Here d_{init} is the initial internal diameter, d_{dia} and d_{sys} are the diastolic and systolic internal model diameters, and P_{dia} and P_{sys} are the diastolic and systolic pressures. Values of d_{dia}, d_{sys}, P_{dia} and P_{sys} were obtained from the dynamic graft FE model analysis. The non-linear stiffening characteristic J was the difference in diameter change per unit pressure from zero to P_{dia} and from P_{dia} to P_{sys}. C_d and d_{dia} were used to calculate the partial objective values for the model, while J was used as a penalty function.

From Eq. (27) a partial objective function formulated for compliance was given by

$$\phi^{\triangle C_d} = \left[1 - \left\{\left|\triangle C_d^{norm}\right|\left(\frac{1}{(m^{\triangle C_d} - 1)}\right)\right\}\right], \tag{29}$$

where

$$\triangle C_d^{norm} = \frac{C_d - C_d^{target}}{C_d^{target}} \tag{30}$$

and

$$m^{\triangle C_d} = \begin{cases} 1 + \left|\frac{C_d^{\max} - C_d^{target}}{C_d^{target}}\right| & \text{for } C_d > C_d^{target} \\ 1 + \left|\frac{C_d^{\min} - C_d^{target}}{C_d^{target}}\right| & \text{for } C_d \leq C_d^{target}. \end{cases} \tag{31}$$

From Eq. (29), $\phi^{\triangle C_d}$ tended to unity as C_d approached C_d^{target}.

The partial objective function for the diastolic diameter was given by

$$\phi^{\triangle d_{dia}} = \left[1 - \left\{\left|\triangle d_{dia}^{Normalized}\right|\left(\frac{1}{(m^{\triangle d_{dia}} - 1)}\right)\right\}\right], \tag{32}$$

where

$$\triangle d_{dia}^{normalized} = \frac{d_{dia} - d_{dia}^{target}}{d_{dia}^{target}}, \tag{33}$$

$$m^{\triangle d_{dia}} = \begin{cases} 1 + \left|\frac{d_{dia}^{\max} - d_{dia}^{target}}{d_{dia}^{target}}\right| & \text{for: } d_{dia} > d_{dia}^{target} \\ 1 + \left|\frac{d_{dia}^{\min} - d_{dia}^{target}}{d_{dia}^{target}}\right| & \text{for: } d_{dia} \leq d_{dia}^{target}. \end{cases} \tag{34}$$

Like Eq. (29), Eq. (32) tended to unity as the model diastolic diameter d_{dia} tended to the target diastolic diameter d_{dia}^{target}.

The parameters $m^{\triangle C_d}$ and $m^{\triangle d_{dia}}$ were multiples used to bias future generations from a certain side. For example, due to tissue ingrowth in the porous grafts, compliance will be reduced after implantation; thus higher compliance values at time of implantation are preferred. These parameters were also used to partially

penalize $\phi^{\triangle C_d}$ and $\phi^{\triangle d_{dia}}$ by making them negative if model C_d or d_{dia} go above or below pre-defined boundary values $C_d^{\max}$and $C_d^{\min}$. Thus,

$$\begin{aligned} &\text{if } \left\{C_d | C_d \leq C_d^{\min} \text{ and } C_d \geq C_d^{\max}\right\} \\ &\text{then } \phi^{\triangle C_d} \text{ was negatively weighted,} \\ &\text{if } \left\{d_{dia} | d_{dia} \leq d_{dia}^{\min} \text{ and } d_{dia} \geq d_{dia}^{\max}\right\} \\ &\text{then } \phi^{\triangle d_{dia}} \text{ was negatively weighted.} \end{aligned} \tag{35}$$

From these partial objective functions an objective function

$$\phi^{GA2} = \frac{\left(w^{C_d} \times \phi^{\triangle C_d^{dyn}}\right) + \left(w^{d_{dia}} \times \phi^{\triangle d_{dia}}\right)}{\left(w^{C_d} + w^{d_{dia}}\right)} \tag{36}$$

was used to calculate the objective value, where $w^{C_d} = 1.75$ and $w^{d_{dia}} = 1.0$ were pre-defined weightings used to bias the objective value to either the compliance or diastolic diameter. From Eq. (36), ϕ^{GA2} tended to unity as $\phi^{\triangle C_d^{dyn}}$ and $\phi^{\triangle d_{dia}}$ tended to unity.

The global penalties used were as follows:

$$\text{If } \begin{cases} C_d \leq 0 \\ C_d = C_d^{target} \\ d_{dia} = d_{dia}^{target} \\ J \leq 0 \end{cases} \text{ then } p^{GA2} = -\infty, \text{ else } p^{GA2} = 1 \tag{37}$$

Equation (37_1) ensured that the FE results gave an expected positive compliance. With Eqs. (37_2) and (37_3), although we were optimizing for C_d^{target} and d_{dia}^{target}, due to numerical errors, such as round-off, these exact solutions will never be achieved. Equation (37_4) ensured that those solutions which did not display nonlinear stiffening were dismissed. Thus these penalties ensured that models which did not converge or do not show nonlinear stiffening were eliminated from future generations, while the partial penalties described by Eqs. (35) and (37) only weight a solution negatively, but do not necessarily expel the solution from future generations.

The fitness function f^{GA2} used to compare the FE solutions obtained was defined by

$$f^{GA2} = p^{GA2} \times \phi^{GA2}. \tag{38}$$

Termination of GA2 was set when a fitness value $f(C, a_i)$ of 0.95 or 50 generations were achieved. Typically, good solutions were found within 35 generations.

4.2 Manufacture and Characterization of Fabrics and Grafts

4.2.1 Manufacture of Fabric Socks

Fabric socks were manufactured using braiding and knitting processes, respectively, (Secant Medical LLC, Perkasie, PA, USA) according to the required specification including longitudinal and circumferential force-displacement characteristics, inner diameter, fabric wall thickness, fiber thickness, pore size and surface coverage. The force-displacement characteristics of the manufactured prototypes were determined experimentally. In an iterative process, the comparison of the experimental data with the numerically predicted requirements was utilized to select the most promising prototype candidates and to guide the manufacturing of subsequent fabric generations.

4.2.2 Mechanical Characterization of Fabric Socks

Longitudinal and circumferential tensile test were conducted using an Instron 5544 universal testing machine (Instron Corp., Norwood, MA, USA) in phosphate-buffered saline solution at 37 °C) to determine the force-displacement relationships in the two principal directions of the fabric socks. For circumferential tests, samples (length: 36.0 mm) were placed over two pins whereas for longitudinal tensile tests, samples (length: 48.0 mm) were clamped flat at both ends using custom-made fabric clamps. The cross-head speed was 200 mm/min [16, 17] for all tests. The samples were tested to a maximum strain of 50 % and 100 % for circumferential and longitudinal tests, respectively. All tests were conducted in accordance with relevant standards [16, 17] as indicated in Sect. 4.1.2.

4.2.3 Manufacture of Graft Samples

Non-reinforced graft samples comprised a 50 mm porous graft sections (manufactured as described in Sect. 3) and two 20 mm e-PTFE graft anastomoses (inner diameter: 4 mm, wall thickness: 30 μm; Atrium, Hudson, NH). The e-PTFE sections anastomosed to the porous graft by repeated application and drying of a polyurethane solution (5 % PUR by mass in Chloroform) while the segments were constrained on a central mandrel. The e-PTFE graft ends ensured a) that graft samples were not damaged due to attachment in the test fixture and b) consistent longitudinal strains during testing. For reinforced grafts, fabric socks were applied over the porous scaffolds ensuring uniformity. At one of the anastomotic regions of the porous graft, the fabric was anastomosed to the structure by additional application of a polyurethane solution (10 % PUR by mass in Chloroform). A higher concentrated polyurethane solution was used to reduce the absorption into the porous structure. Once this anastomotic region was cured, the fabric sock was

strained, by uniformly and evenly stretching the fabric over the graft sample to the required amount and fixed to the porous graft by again applying repeated layers of polyurethane solution.

4.2.4 Compliance Testing of Grafts

In vitro static and dynamic compliance tests were conducted using a custom-built test rig featuring a closed flow loop system (phosphate buffered saline, 37 °C) [29]. For static tests, the range of the internal pressure was 0–200 mmHg. For dynamic tests, pressure of 80–120 mmHg or equivalent pressure values accounting for the luminal latex liner (as described further below in this section). The outer diameter of the graft samples was monitored with macroscopic digital imaging (Leica MS5 stereo microscope (Leica, Wetzlar, Germany), Sony CCD-IRIS digital camera (Sony, Tokyo, Japan), Strata Videoshop (Strata, Santa Clara, UT, USA)). The compliance was determined using the inner diameter values. These were calculated from the measured outer graft diameter, the wall thickness and numerically predicted wall compression. In addition, compliance was based on the outer graft diameter for selected experiments for comparison purposes. Custom-made latex liners (outer diameter: 3.62 ± 0.15 mm, wall thickness: 0.19 ± 0.02 mm; Roynhardt Pvt. Ltd., Johannesburg, South Africa) were inserted into the graft samples to prevent pressure loss due to the scaffold porosity during the test procedure. The stiffening effect of the latex liner was compensated using the following procedure during a preliminary static compliance test for each graft sample:

1. Subtraction of pressure-diameter curves of the latex liner from the pressure-diameter curves of the graft sample with latex liner.
2. Calculation of equivalent pressure values for the graft-liner samples corresponding to diastolic and systolic pressure of 80 and 120 mmHg for a graft sample without latex liner.

The equivalent diastolic-systolic pressure values used in dynamic compliance tests were 126–203, 144–218 and 163–243 mmHg for the non-reinforced graft samples and 83–128, 102–150 and 116–168 mmHg for the fabric-reinforced samples (for porogen size groups of 90–106, 106–125 and 125–150 μm, respectively).

4.3 Non-Reinforced Porous Graft Predictions

Table 3 gives the dynamic and static compliance values obtained from the graft numerical models for each of the porous graft structures without fabric reinforcing. Other values displayed include wall compression and diastolic and systolic internal diameters. As expected, compliance increases with increased pore size. Little difference was observed between the dynamic and static compliance values;

Table 3 Numerical predictions for diametric compliance, internal diameter, and wall compression of non-reinforced graft models for static and dynamic loading

Porogen size (μm)	90–106	90–106	106–125	106–125	125–150	125–150
Loading type	Stat	Dyn	Stat	Dyn	Stat	Dyn
C_d (%/100 mmHg)	16.9	16.0	20.3	19.2	33.9	31.5
Internal diameter ϕ_i (mm)						
Diastolic	4.088	4.064	4.160	4.133	4.378	4.342
Systolic	4.377	4.319	4.516	4.445	5.002	4.879
Wall compression (%)						
Diastolic	5.46	1.91	6.25	1.97	8.31	1.28
Systolic	7.72	5.68	8.99	6.51	13.06	8.77

however, as pore size increased, a slight increase was seen in static compliance. Diastolic and systolic internal diameters reflected similar characteristics with respective static and dynamic compliance. However, there was a large difference between the static and dynamic wall compression values obtained; for dynamic values the compression observed was much lower, due to the lagging wall response with pulsatile pressure. Figure 10a–c displays the dynamic circumferential, radial and axial stress fields through the various pore size non-reinforced graft structures at mean internal pressure (100 mmHg). The stress fields and sizes are displayed to the same scale to highlight the difference in field and diameters. The profiles of circumferential, radial and axial stress are illustrated in Fig. 10d–f for the various porogen size non-reinforced graft structures. The contour plots and graphs in Fig. 10 indicate that the circumferential stress increased with increased pore size, with the difference between the 90–106 and 106–125 μm being less than that observed between the 106–125 and 125–150 μm. The magnitude of the radial stress for each pore size group was equal through the wall thickness. It was also observed that the axial stress fields decreased considerably in magnitude with increased pore size. The shape of the circumferential and radial stress profiles through the graft wall were similar for increasing pore size. However, a variation in axial stress profiles was observed between the pore size grafts. The stronger 90–106 μm porogen size graft had a higher axial stress at the luminal surface which decayed towards the adventitial surface, while the axial stress profiles through the wall were almost constant for the weaker 106–125 and 125–150 μm. Thus, the weaker large pore sized grafts appeared to distribute the axial load more evenly through the wall.

4.4 Optimised Reinforced Graft Solutions

A total of 39 and 34 generations were required before model solutions the desired 0.95 fitness value were obtained for the 106–125 and 125–150 μm porogen size, respectively. For the 90–106 μm graft type, the full 50 generations were needed before the model reached a fitness value 0.948. The results obtained from GA2 gave

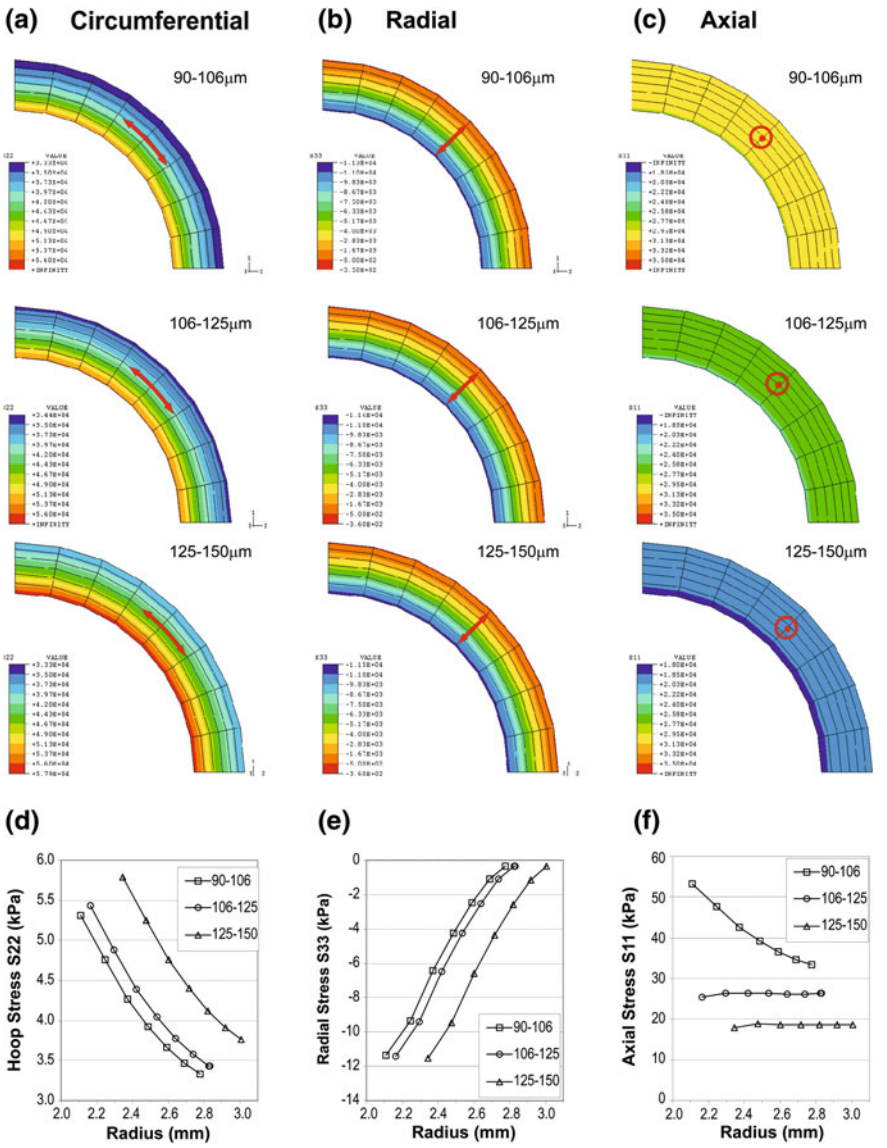

Fig. 10 Contour plots and graphs showing the stress variation through the wall thickness of 90–106, 106–125 and 125–150 μm porous grafts at a luminal pressure of 100 mmHg: Circumferential stress (**a**, **d**), radial stress (**b**, **e**), axial stress (**c**, **f**)

dynamic diameter compliance values of 6.4, 6.9 and 7.1 %/100 mmHg and diastolic diameters of 3.965, 3.998 and 4.000 mm for the fabric reinforced 90–106, 106–125 and 125–150 μm porogen grafts, respectively. A maximum wall compression of 6.20 % was observed for the 125–150 μm porogen graft. The circumferential strain

Table 4 Optimal solutions for fabric reinforced porous grafts of 90–106, 106–125 and 125–150 μm porogen size class

Graft porogen size (μm)	90–106	106–125	125–150
Dynamic C_d (% /100 mmHg)	6.4	6.9	7.1
Internal diameter ϕ_i (mm)			
Diastolic	3.965	3.998	4.000
Systolic	4.067	4.109	4.113
Wall compression (%)			
Diastolic	2.93	3.24	3.82
Systolic	4.82	5.31	6.20
Fabric circumferential strain (%)			
Diastolic	6.61	7.19	7.08
Systolic	8.13	8.85	8.70
Fabric model coefficients			
C	607.969	977.145	3881.518
a_1	0.028	15.885	17.748
a_2	270.643	204.607	133.838
a_3	1.719	21.012	6.662
a_4	24.310	16.631	25.734
a_5	2.745	−28.013	13.785
a_6	64.376	50.642	66.498
a_7	8.014	−24.693	−18.083
a_8	−8.797	−13.284	2.018
a_9	−9.155	14.190	20.619
Fitness value $f(C, a_i)$	0.9484	0.9552	0.9509
Objective value $\phi(C, a_i)$	0.9484	0.9552	0.9509
Partial objective values			
$\phi^{\triangle C_d^{dyn}}$	0.9693	0.9329	0.9230
$\phi^{\triangle d_{dia}}$	0.9119	0.9943	0.9996
Generation number	50	39	34

in the fabric reinforcement was greatest for the reinforced 106–125 μm porogen graft, with a value of 8.85 %, while values of 8.13 % and 8.70 % were observed for the reinforced 90–106 and 125–150 μm porogen grafts, respectively. In contrast, the internal diameter at the systolic pressure was less for the 90–106 and 106–125 μm grafts than for the 125–150 μm porogen graft, implying that the adventitial reinforcing fabric plays a larger role in the weaker structures, or increased pore size. Table 4 displays the optimal fabric model solutions obtained from GA2 for each of the pore size grafts.

Figure 11 displays the dynamic circumferential, radial and axial stress through the wall thickness for the various pore size adventitial fabric reinforced grafts at mean pressure (100 mmHg). The high fabric stress values, indicated by the sharp change in stress profile in Fig. 11d, f, obtained for the 125–150 μm reinforced graft compared to the 106–125 and 90–106 μm structures, illustrated that the fabric reinforcing played a dominant role in the weaker 125–150 μm graft, while this role was reduced in the 106–125 and 90–106 μm structures. Comparing Fig. 10d–f and

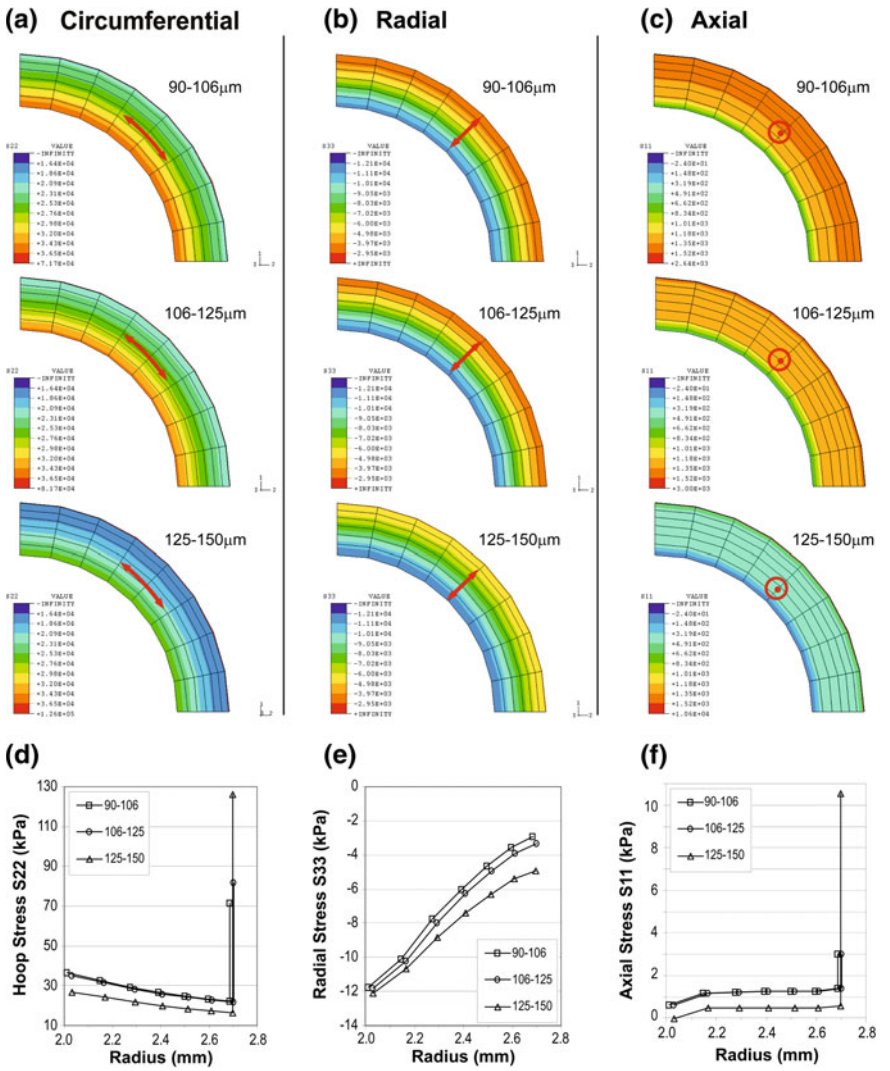

Fig. 11 Contour plots and graphs showing the stress variation through the wall thickness of 90–106, 106–125 and 125–150 μm porous grafts with adventitial fabric reinforcement at a luminal pressure of 100 mmHg: Circumferential stress (**a**, **d**), radial stress (**b**, **e**), axial stress (**c**, **f**)

Fig. 11d–f, the fabric reinforcing reduced and levelled out the circumferential stresses for all porogen sizes. The axial stress was similarly reduced for all porogen sizes whereas levelling out of axial stress was only observed in the 125–150 μm graft but not in the 106–125 and 90–106 μm structures. With the addition of the reinforcing, the compressive radial stress increased toward the outer (adventitial) surface, while relatively small changes were observed at the lumen for all graft types.

The three highest ranked fabric model solutions were implemented in the circumferential and longitudinal tensile numerical models to obtain the fabric requirements in terms of force per unit length vs. displacement for porous grafts of each porogen size group. These curves were used to develop physical fabrics.

In an iterative process, the comparison of the experimental data with the numerically predicted requirements was utilized to select the most promising prototype candidates and to guide the manufacturing of subsequent fabric generations. From an initial generation of 16 different fabric socks, six designs were identified as potential candidates to comply with the required specification with respect to force-displacement characteristics and promotion of tissue ingrowth. A refined evaluation resulted in exclusion of four of the six fabric sock designs from further review. The short-listed two designs underwent two iterations of design adjustment, manufacturing and experimental assessment. The final generation of the two prototype designs (prototypes I and II) featured knits of Dacron fibre threads (fibre diameter: 50 μm) with pore diameter of 0.35 mm and surface coverage of 70–75 %. To enable a feasible assembly procedure of the fabric sock and the porous graft structure (OD: 5.0 mm), it was found that an inner diameter of the fabric socks of 6.0 mm was preferential to the value of 5.0 mm predicted numerically. The difference in inner diameter of the sock and outer diameter of the graft was accommodated by longitudinally stretching the fabric sock by $59 \pm 1.9\,\%$ (prototype I) and $91 \pm 1.7\,\%$ (prototype II) during the assembly procedure. Figure 12a displays the circumferential force-displacement curves of the two prototype socks, without (i.e. as manufactured) and with longitudinal pre-strain, and the optimal fabric model solution for the graft of 90–106 μm porogen size. Figure 12b, c displays experimental data and optimised model solutions with pre-straining. The models represented the physical behaviour of the fabrics very well in circumferential direction (Fig. 12b). For longitudinal tension (Fig. 12c), the agreement between model and experiment was reasonable for longitudinal strains up to approximately 60 %.

Using these fabric model solutions, the FE model for fabric-reinforced grafts predicted compliance values that deviated from those obtained with the optimal fabric model solutions (see Table 4). Table 5 presents the static and dynamic compliance values numerically, predicted and experimentally measured, for non-reinforced grafts and grafts reinforced with prototype I fabric socks. For the compliance based on inner graft diameter, $C_{d,dyn}$(ID) and $C_{d,stat}$(ID), the numerical models markedly overestimated the compliance in all cases. The overestimation was more pronounced in the fabric-reinforced grafts compared to the non-reinforced grafts, except for the largest porogen size class 125–150 μm. The variation between numerical and experimental values increased with increasing porogen size for the non-reinforced grafts whereas the variation decreased with increasing porogen size for the fabric-reinforced grafts. A considerably better agreement between numerical and experimental results was obtained when the compliance, $C_{d,stat}$(OD), was calculated using the outer diameter of the graft. This was demonstrated for the static case. The improvement was more apparent for the non-reinforced grafts compared to the reinforced grafts.

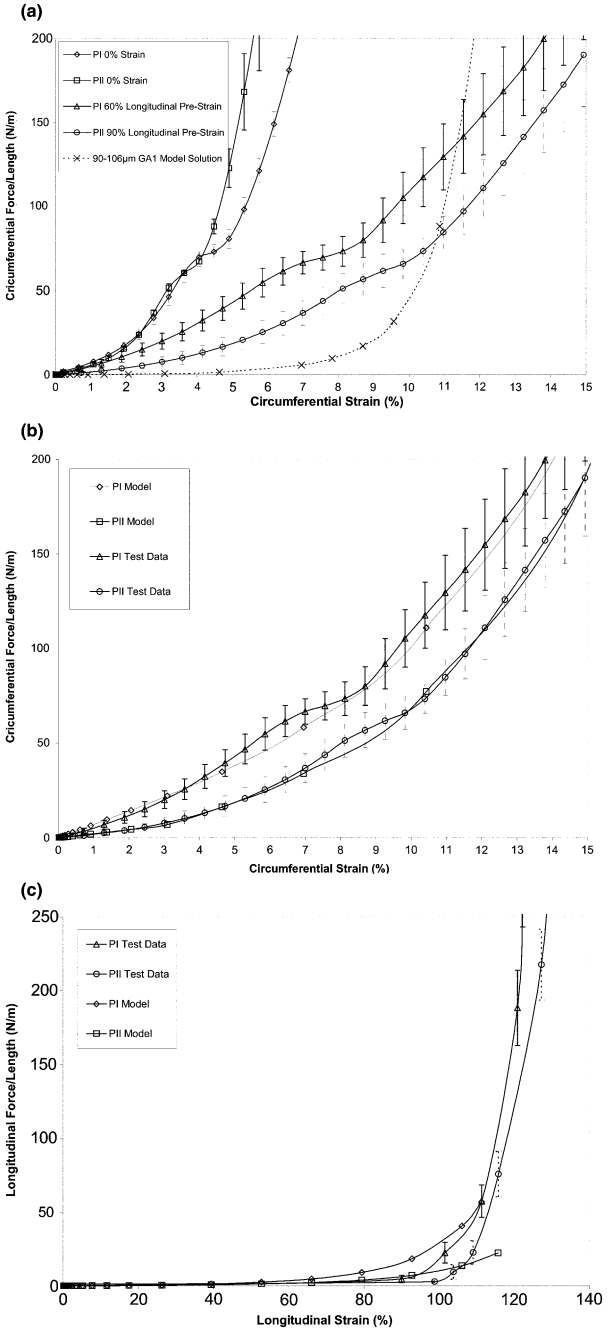

Fig. 12 Experimental and numerical data for the final fabric sock prototypes I (PI) and II (PII): **a** Force-displacement curves from circumferential tensile tests of the samples without and with longitudinal pre-strain and the optimal fabric model solution for 90–106 μm porogen size graft, **b** Fabric model solutions and experimental data for circumferential tensile tests of pre-strained fabric samples, **c** Fabric model solutions and experimental data for longitudinal tensile tests of pre-strained fabric samples

Table 5 Static ($C_{d,stat}$) and dynamic ($C_{d,dyn}$) compliance of non-reinforced and prototype I fabric-reinforced graft samples from in vitro compliance tests (Experiment) and numerical predictions (Model)

	Non-reinforced grafts			Fabric-reinforced grafts		
Porogen size (μm)	90–106	106–125	125–150	90–106	106–125	125–150
$C_{d,dyn}$ (ID)						
Experiment	13.3 ± 1.2	12.7 ± 2.9	15.5 ± 1.3	2.1 ± 0.8	3.0 ± 2.4	4.0 ± 0.7
Model	16.0	19.2	31.5	5.3	5.5	6.0
$C_{d,stat}$ (ID)						
Experiment	13.0 ± 2.4	12.9 ± 7.8	16.4 ± 4.6	1.3 ± 1.2	2.5 ± 3.3	4.1 ± 4.9
Model	16.9	20.3	33.9	5.5	5.8	6.2
$C_{d,stat}$ (OD)						
Experiment	10.1 ± 1.9	9.7 ± 5.9	12.2 ± 3.9	0.5 ± 0.7	1.7 ± 2.1	2.4 ± 4.5
Model	9.7	9.8	14.2	2.0	2.8	2.0

The compliance values were based on inner graft diameter (ID) for the dynamic case and both inner (ID) and outer (OD) graft diameter for the static case. All values given in %/100 mmHg

5 Discussion

The objective of this study was to find an optimal structural design of a tissue-regenerative vascular prosthesis exhibiting arterial-like mechanics. Adopting from native arteries a layered structure of intima/media and adventitia, the challenge was to identify the mechanical characteristics of an adventitial fabric layer that provide together with the given properties of a porous polymeric intima/media layer the desired biomechanical properties of the graft structure. It was shown that by combining finite element methods and genetic algorithms, complemented with experimental methods, the required mechanical characteristics of the adventitial fabric reinforcement can be specified. The finite element methods were used to study the structural mechanics of the two-layer graft system, whereas the genetic algorithms served to optimize the mechanical characteristics of the adventitial fabric. As part of this numerical framework, experimental methods were employed to determine constitutive material parameters. Beyond the demonstration of the feasibility of numerical method, it was shown that the graft system of adventitially reinforced polymer with well-defined interconnected porosity can be expected to facilitate the ingrowth and regeneration of tissue such as arterioles, endothelial cells and smooth muscle cells for all pore sizes studied.

With respect to vascular tissue engineering, wall compression at systolic pressure (during dynamic loading) was predicted to be 5.68, 6.51, and 8.77 % in non-reinforced porous grafts (Table 3) and 4.82, 5.31, and 6.20 % in the fabric reinforced grafts (Table 4) for the 90–106, 106–125, and 125–150 μm porogen size group. These values represented a reduction of wall compression in the reinforced grafts by 15.2, 18.4, and 29.3 % compared to the non-reinforced grafts of the three porogen size groups. Considering that the predicted dilation was larger in the non-reinforced grafts compared to the reinforced grafts, these findings indicated that

the wall compression was predominantly governed by the dilation of the graft inducing transverse wall contraction. The compression of the wall due to internal pressure load played a secondary role even in samples with fabric reinforcement. The reduced wall compression in reinforced samples also suggested that the fabric reinforcement contributed to maintaining the dimensions of the interconnected pores required for tissue ingrowth. The diameter of interconnecting pore windows was on average $0.52 \pm 0.04\,\%$ of the porogen diameter [1]. For the porous grafts of the 90–106, 106–125, and 125–150 μm porogen size, the minimum pore window diameter was approximately 47, 55, and 65 μm. With the predicted wall compression at systolic pressure, the minimum pore window sizes, available for cellular ingrowth, decreased to 44, 52, and 59 μm in the non-reinforced porous grafts feature (while the minimum window size was slightly larger in the reinforced porous structures due to the lower wall compression). The average diameter of a capillary is 8–10 μm, while the diameter of a functional arteriole, endothelium and a single layer of smooth muscles is in the order of 30 μm [7, 8]. Thus, all three pore size graft groups permit ingrowth of arterioles, endothelial cells and smooth muscle cells.

The comparison with experimental results indicated that the numerical solutions predicted higher values for the graft compliance for most of the cases studied. For the non-reinforced grafts it was observed that a considerably improved agreement between model and experiment was achieved when the outer graft diameter, instead of the inner diameter, was used for compliance calculations. The relative differences decreased from 64.7 ± 38.9 to $4.5 \pm 10.6\,\%$ (average for the three porogen size groups). For the fabric-reinforced grafts, the relative differences observed were larger and the change of diameter reference resulted in a less pronounced improvement from 168.8 ± 139.6 to $116.0 \pm 164.4\,\%$. The best agreement for reinforced grafts was however achieved for the dynamic compliance with $95.2 \pm 52.2\,\%$. In view of the markedly different compliance values for the non-reinforced and the fabric-reinforced grafts, the absolute differences between experiments and models were reviewed additionally. For the dynamic compliance based on inner diameter, the model predictions exceeded the experimental results on average by a mere $2.6 \pm 0.6\,\%/100$ mmHg for the grafts with fabric reinforcement and by $8.4 \pm 6.9\,\%/100$ mmHg for the non-reinforced grafts. These values indicated in fact an acceptable agreement, in particular for the fabric-reinforced grafts. For the static compliance associated with the change of inner diameter, the absolute difference decreased to similar values of $0.7 \pm 1.0\,\%/100$ mmHg and $0.6 \pm 1.3\,\%/100$ mmHg for the reinforced and the non-reinforced grafts, respectively. Despite the satisfactory agreements of the absolute differences, various factors were identified as potential contributors to the observed deviations. The fabric models did not optimally represent the physical behaviour of the fabric prototypes I and II in longitudinal tension for strains exceeding 60 %, see Fig. 12c. In addition, the fabric model solutions were not optimized for transverse strain due to lack of experimental data for the fabric samples. The mechanical characterization of the porous polymer was performed on samples prepared from cast rods as compared to the grafts which were cast as tubes. This

may have caused different material/structural properties due to potentially varying packing configurations of the porogen. The latex liners obtained and used for compliance testing of the graft samples displayed a variation in mechanical properties. Furthermore, applying longitudinal strain to the graft samples according to the protocols for compliance testing may have caused the luminal latex liners to collapse inside the graft sample affecting the graft's behaviour. An appreciable variation of the experimental results, indicated by the large standard deviations of the measured compliance values (Table 5), may also be attributed to the intensive manual processes during manufacturing of the graft samples.

While the presented problem focused on the optimization of a fabric-type layer, the numerical solutions may be applied to other materials and structures, functioning as an adventitial reinforcement. Furthermore, the numerical method offers potential for the application to optimization problems with different concepts of modular, or composite, vascular prostheses. This may, in particular with emphasis on tissue regeneration, include the consideration of the biodegradation of the prosthetic materials and the incorporation of tissue in the initial mechanical design of vascular prostheses.

Acknowledgments This work was mainly funded through a research collaboration grant by Medtronic Inc. (Minneapolis, MN, USA) to the University of Cape Town. The authors acknowledge the assistance of Richard Steventon with the GA coding.

References

1. Bezuidenhout, D.: Porous Polymeric Superstructures as In-Growth Scaffolds for Tissue-Engineered Vascular Prosthesis. Ph.D. Thesis, Stellenbosch University, 2001
2. Bezuidenhout, D., Davies, N., Zilla, P.: Effect of well defined dodecahedral porosity on inflammation and angiogenesis. ASAIO J. **48**, 465–471 (2002)
3. Burkel, W.E: The challenge of small diameter vascular grafts. Med. Prog. Technol. **14**, 165–175 (1988)
4. Chuong, C.J, Fung, Y.C: Three-dimensional stress distribution in arteries. J. Biomech. Eng. **105**, 268–274 (1983)
5. Davies, N., Dobner, S., Bezuidenhout, D., Schmidt, C., Beck, M., Zisch, A.H., Zilla, P.: The dosage dependence of VEGF stimulation on scaffold neovascularisation. Biomaterials **29**, 3531–3538 (2008)
6. Deutsch, M., Meinhart, J., Zilla, P., Howanietz, N., Gorlitzer, M., Froeschl, A., Stuempflen, A., Bezuidenhout, D., Grabenwoeger, M.: Long-term experience in autologous in vitro endothelialization of infrainguinal ePTFE grafts. J. Vasc. Surg. **49**, 352–362 (2009)
7. Fung, Y.C: Biomechanics: Mechanical Properties of Living Tissue, 2nd edn. Springer, New York (1984)
8. Gamble, J., Matthias, L., Meyer, G., Kaur, P., Russ, G., Faull, R., Berndt, M., Vadas, M.: Regulation of in vitro capillary tube formation by anti-integrin antibodies. J. Cell Biol. **121**, 931–943 (1993)
9. Hasson, J.E., Megerman, J., Abbott, W.A: Increased compliance near vascular anastomosis. J. Vasc. Surg. **2**, 419–423 (1985)
10. Hayashi, K.: Experimental approaches on measuring the mechanical properties and constitutive laws of arterial walls. J. Biomech. Eng. **115**, 481–487 (1993)

11. Hess, F., Jerusalem, C., Braun, B.: The endothelialisation of a fibrous polyurethane microvascular prosthesis after implantation in the abdominal aorta of the rat. J. Cardiovasc. Surg. **24**, 516–524 (1983)
12. How, T.V., Guidon, R., Young, S.K: Engineering design of vascular prosthesis. Proc. Inst. Mech. Eng. [H] **206**, 61–71 (1992)
13. Hsu, C.-C., Chao, C.-K., Wang, J.-L., Lin, J.: Multiobjective optimization of tibial locking screw design using a genetic algorithm: evaluation of mechanical performance. J. Orthop. Res. **24**, 908–916 (2006)
14. Khalil, A.S., Bouma, B.E., Kaazempur Mofrad, M.R: A combined FEM/genetic algorithm for vascular soft tissue elasticity estimation. Cardiovasc. Eng. **6**, 93–103 (2006)
15. Kim, J.H.: Fabric Mechanics Analysis Using Large Deformation Orthotropic Shell Theory. Ph.D. Thesis, North Carolina State University, 1991
16. NN: Cardiovascular Implants—Vascular Prosthesis. American National Standard Association for the Advancement of Medical Instrumentation, AAMI standard edition, 1994
17. NN: Cardiovascular Implants—Tubular Vascular Prosthesis. ISO International Standard 7198, 1998
18. Pandit, A., Lu, X., Wang, C., Kassab, G.S.: Biaxial elastic material properties of porcine coronary media and adventitia. Am. J. Physiol. Heart Circ. Physiol. **288**, H2581–H2587 (2005)
19. Seifert, K.B., Albo, D., Knowlton, H., Lyman, D.J: Effect of elasticity of prosthetic wall on patency of small-diameter arterial prosthesis. Surg. Forum **30**, 206–208 (1979)
20. Siauve, N., Nicolas, L., Vollaire, C., Marchal, C.: Optimization of the sources in local hyperthermia using a combined finite element-genetic algorithm method. Int. J. Hyper. **20**, 815–833 (2004)
21. Stewart, S.F.C, Lyman, D.J: Effects of vascular graft/natural artery compliance mismatch on pulsatile flow. J. Biomech. **25**, 297–310 (1992)
22. Storåkers, B.: On material representation and constitutive branching in finite compressible elasticity. J. Mech. Phys. Solids **34**, 125–145 (1986)
23. Tai, N.R., Salacinski, H.J., Edwards, A., Hamilton, G., Seifalian, A.M: Compliance properties of conduits used in vascular reconstruction. Br. J. Surg. **87**, 1516–1524 (2000)
24. Takahara, A., Coury, A.J., Hergenrother, R.W., Cooper, S.L: Effect of soft segment chemistry on the biostability of segmented polyurethanes. I. In vitro oxidation. J. Biomed. Mater. Res. **25**, 341–356 (1991)
25. Wang, C., Garcia, M., Lu, X., Lanir, Y., Kassab, G.S.: Three-dimensional mechanical properties of porcine coronary arteries: a validated two-layer model. Am. J. Physiol. Heart Circ. Physiol. **291**, H1200–H1209 (2006)
26. Weston, M.W., Rhee, K., Tarbell, J.M: Compliance and diameter mismatch affect the wall shear rate distribution near end-to-end anastomosis. J. Biomech. **29**, 187–198 (1996)
27. Yeoman, M.S., Reddy, B.D., Bowles, H.C., Bezuidenhout, D., Zilla, P., Franz, T.: A constitutive model for the warp-weft coupled non-linear behavior of knitted biomedical textiles. Biomaterials **31**(32), 8484–8493 (2010)
28. Yeoman, M.S., Reddy, B.D., Bowles, H.C., Zilla, P., Bezuidenhout, D., Franz, T.: The use of finite element methods and genetic algorithms in search of an optimal fabric reinforced porous graft system. Ann. Biomed. Eng. **37**, 2266–2287 (2009)
29. Yeoman, M.S.: The Design and Optimisation of Fabric Reinforced Porous Prosthetic Grafts Using Finite Element Methods and Genetic Algorithms. Ph.D. Thesis, University of Cape Town, June 2004
30. Zilla, P., Bezuidenhout, D., Human, P.: Prosthetic vascular grafts: Wrong models, wrong questions and no healing. Biomaterials **28**, 5009–5027 (2007)

http://www.springer.com/978-3-642-53835-3

Cardiovascular and Cardiac Therapeutic Devices
Franz, Th. (Ed.)
2014, VIII, 243 p. 91 illus., Hardcover
ISBN: 978-3-642-53835-3